PCCP

PAPER

View Article Online
View Journal | View Issue

Cite this: *Phys. Chem. Chem. Phys.*, 2016, **18**, 33158

Study of the interplay between N-graphene defects and small Pd clusters for enhanced hydrogen storage *via* a spill-over mechanism†

E. Rangel,*[a] E. Sansores,[b] E. Vallejo,[a] A. Hernández-Hernández[a] and P. A. López-Pérez[a]

Received 21st September 2016,
Accepted 16th November 2016

DOI: 10.1039/c6cp06497c

www.rsc.org/pccp

The hydrogen spill-over mechanism was studied by applying Density Functional Theory. We used small palladium clusters to act as the catalyst supported on the substrate (comprised of pyridinic and pyrrolic nitrogen doped graphene), in order to study hydrogen dissociation, migration and diffusion. Charge transfer and strong binding between the catalyst and the substrate lead to dissociated states of H_2 and prevent clusters from detaching and coalescing. In dissociated cases of H_2 on Pd clusters, energy barriers below 0.6 eV were found. Likewise, concerning hydrogen migration from the catalyst to the substrate, energy barrier values of 0.8 eV (pyridinic defect) and 0.5 eV (pyrrolic defect) were apparent in the case of the Pd_4 cluster at full hydrogen saturation. This indicates that hydrogen dissociation and migration may occur spontaneously at room temperature. This result shows that the interaction between the defects and the small metal clusters may explain the role that defects play in hydrogen migration from the catalyst to the substrate. Subsequently, it was found that thermal desorption does not limit chemisorbed hydrogen diffusion on the substrate. This work may thus help to determine experimental strategies with the capacity to enhance hydrogen storage.

1. Introduction

In order to assess the problem of hydrogen storage on graphene, it has been undertook considerable theoretical and experimental research, focussing on this problem in solids.[1–5] The motivation for these efforts was to achieve hydrogen storage to serve as a vehicle fuel, in a safe and efficient way. Hydrogen storage requires: (1) high gravimetric and volumetric densities (6 wt% or more[6] for gravimetric density and 62 kg m^{-3} of H_2 for volume density), (2) low H_2 sorption temperature, (3) fast reaction kinetics, and (4) good reversibility. However at room temperature, the low or null hydrogen molecular storage capacity of pure graphene, in addition to the high energetic cost for obtaining hydrogenated graphene *via* dissociation of H_2, limits their use in practical storage systems.[7–11]

The hydrogen spill-over mechanism offers an effective way to enhance hydrogen storage on adsorbent materials. Hydrogen spill-over is defined as the dissociative adsorption of H_2 on metal catalyst particles, followed by the migration of H atoms to the substrate.[12] However, the mechanism of spill-over storage is still far from being fully understood and further investigation from a fundamental point of view is significantly important. In fact, recent experimental studies have reported that hydrogen spill-over offers a viable technique for achieving ample hydrogen storage on different carbon based materials.[13–22]

Density Functional Theory (DFT) however was used by Wu *et al.*[23] and Psofogiannakis and Froudakis[24] to calculate the energy barrier for hydrogen migration from the Pt_4 cluster to the carbon surface. Energy barriers of 2.7 eV (Wu *et al.*[23]) and 2.6 eV (Psofogiannakis and Froudakis[24]) were obtained. Notably, other authors recently applied density functional theory to study the hydrogen spill-over mechanism on Pd_6 and Pd_{13} clusters, supported on graphene. They found an energy barrier of 2.7 eV inhibiting migration from the catalyst to the graphene, in the case of dissociated H atoms on the Pd_{13} cluster.[25] These results suggest that the migration of hydrogen is thermodynamically and kinetically very difficult. Under normal conditions hydrogen spill-over thus would not occur, making it a rare event.

Although extensive research has been undertaken to elucidate the hydrogen spill-over mechanism, there is no general consensus to date that satisfactorily explains the mechanism, which results in the observed large storage capacity (up to 4.4 wt% of H_2) and

[a] *Escuela Superior de Apan, Universidad Autónoma del Estado de Hidalgo, Carretera Apan-Calpulalpan Km. 8, Col. Chimalpa, C.P. 43920, Apan, Hidalgo, Mexico. E-mail: kovoldedu@yahoo.com.mx*

[b] *Instituto de Investigaciones en Materiales, Universidad Nacional Autónoma de México, Apartado Postal 70-360, C.P. 04510, México, D. F., Mexico*

† Electronic supplementary information (ESI) available. See DOI: 10.1039/c6cp06497c

the hydrogen desorption of the carbon based storage compounds at room temperature.[26]

A theoretical study of the hydrogen spill-over mechanism of small platinum clusters supported on carbon nanotubes was presented by Juarez-Mosqueda *et al.*[27] They proposed that the observed saturation of carbon nanotubes at hydrogen background pressure (in the hydrogen spill-over process) occurs through mobile Pt nanoclusters. Nevertheless, the high mobility of the Pt nanoparticles on the substrate represents a disadvantage. The Pt particles tend to coalesce into larger clusters, which ultimately terminate the efficiency of the catalyst. Consequently, the formation of large clusters should be avoided if possible. Another problem is the competition between the desorption of metal–hydrogen complexes and H_2, and the migration of hydrogen from the catalyst to the substrate. This problem can be avoided by increasing the binding energy between the metal clusters and the supporting carbon substrate.

For this reason, nitrogen doping has proven to be an effective way to adjust graphene properties and facilitate its possible use in different applications.[28] The decoration of Pd nanoparticles on nitrogen doped graphene was recently studied by Parambhath *et al.*[26] They detected high dispersion and strong binding between Pd nanoparticles. Nitrogen-doped graphene can also be used to enhance graphene capacity for hydrogen uptake. A maximum hydrogen capacity of 4.4 wt% was achieved at 25 °C and at a pressure of 4 MPa. Based on these experimental details, we recently studied the first step in the hydrogen spill-over mechanism. We found dissociated states of H_2 on Pd clusters, supported on pyridinic nitrogen doped graphene. We concluded that this process may occur spontaneously at room temperature.[29]

Due to computational limitations, the present study only deals with small Pd clusters at the subnanoscale (Pd_n, n = 1–4). Furthermore, the effect of the cluster size on hydrogen migration and diffusion was not studied. This matter will be studied in the future. Although we used small clusters in our calculations (compared to experimental real size catalyst particles), previous studies have shown that at full saturation (of H atoms on Pd clusters anchored on graphene vacancies) the hydrogen dissociative chemisorption energy threshold does not vary significantly according to the cluster size.[30,31]

Several groups have also observed three different nitrogen doped graphene systems: (1) pyridinic, (2) pyrrolic and (3) graphitic defects.[32–38]

Based on experimental details,[26] some important questions emerge: (1) what kinds of interactions occur between palladium atoms and N-graphene defects? (2) If Pd atoms nucleate into three-dimensional clusters, what is the smallest Pd cluster with a three-dimensional structure? (3) Does the hydrogen spill-over mechanism satisfactorily explain the observed large storage capacity, up to 4.4 wt% of H_2? (4) Does the interaction between the defects and metal clusters adequately explain the role that defects play in hydrogen migration from the catalyst to the substrate?

The objectives of this work are: (1) to study the viability of hydrogen spill-over as a mechanism for storing hydrogen. (2) To define whether the interaction between the defects and metal clusters can explain the role that defects play in hydrogen migration from the catalyst to the substrate. (3) To investigate the competition between the chemisorbed hydrogen diffusion and thermal desorption. (4) To study the hydrogen spill-over mechanism in small palladium clusters (Pd_n, n = 1–4) supported on pyridinic and pyrrolic nitrogen doped graphene.

This article is organized as follows: method is presented in Section 2, our results are discussed in Section 3 and finally the main conclusions are summarised in Section 4.

2. Method

Density functional theory was used within the general gradient approximation (GGA)[39] and the Quantum Espresso code.[40] We used the norm conserving Troullier–Martins[41] pseudopotentials in the fully separable form of the Kleinman–Bylander[42] and Perdew–Burke–Ernzerhof (PBE) expression[43] for exchange correlation energies. It is well-known that GGA or meta-GGA type calculations usually underestimate transition state barriers. In fact, the former reactions exhibit mean absolute errors greater than ≥ 0.13 eV (3 kcal mol^{-1}).[44] In contrast, very high accuracy is available for gas-phase reactions with hybrid functionals.[45] Notably, the HSE06 functional agrees reasonably well with the Random Phase Approximation (RPA).[45] Therefore, to verify the accuracy of the PBE functional, we performed an additional calculation using the hybrid Heyd–Scuseria–Ernzerhof screened Coulomb potential hybrid functional (HSE),[46] with α = (the mixing parameter) and ω = 0.11 a.u.$^{-1}$ (the range for the screened exchange interaction). This functional is usually referred to as HSE06. Due to high computational costs, only single-points in the reaction paths were recalculated. Likewise, the hybrid density functional was validated with calculations of the structural properties of palladium (see the ESI†). This formalism is accurate enough to reproduce the electronic properties of chemisorbed species. However, it cannot describe the physisorption regime, because the non-local correlation effects needed to address the dispersion interactions are not included. Besides this, errors associated with DFT formalism at large distances and associated with dispersion interactions are somewhat smaller than those involved in making or breaking chemical bonds.

We studied the minimum energy path (MEP) together with the nudged elastic band (NEB) method and the conjugate gradient technique,[39,47] in order to find local minima. To verify the accuracy of the PBE functional (GGA) (for different reactions of hydrogen migration from the catalyst to the substrate), several points in the reaction paths using the hybrid HSE functional were recalculated. More details about the transferability of pseudopotentials, magnetic moment, total charge of nitrogen and C–N bonds (see Table S1) and simulation details are provided in the ESI.†

The defect formation energy (ΔE_f) eqn (1),[48] and the adsorption energies of Pd-metal atoms ($E_{ad_{Pd}}$) eqn (2), hydrogen molecules $\left(E_{ad_{H_2}}\right)$ eqn (3) and the complex $Pd_n\nu H$ $\left(E_{ad_{Pd_n\nu H}}\right)$ eqn (4) were computed as:

$$\Delta E_f = E_{(GN_xV_y+Pd_n)} + (x+y)\mu_c - (E_G + x\mu_N + nE_{Pd_{n=1}}) \quad (1)$$

$$E_{ad_{Pd}} = E_{GN_xV_y} + E_{Pd_n} - E_{(GN_xV_y+Pd_n)} \quad (2)$$

$$E_{ad_{H_2}} = E_{(GN_xV_y+Pd_n)} + E_{zH_2} - E_{(GN_xV_y+Pd_n+zH_2)} \quad (3)$$

$$E_{ad_{Pd_nvH}} = E_{GN_xV_y} + E_{Pd_nvH} - E_{(GN_xV_y+Pd_nvH)} \quad (4)$$

$$\Delta E_j = E_{(GN_xV_y+Pd_n+vH)_j} - E_{(GN_xV_y+Pd_n+vH)_{initial}} \quad (5)$$

Finally, the reaction path was calculated as the difference in the total energies eqn (5).

In this context, N_xV_y represents the defect. x is the number of carbon atoms substituted by N nitrogen atoms and y is the number of V vacancies. $x + y$ is the number of total carbon atoms removed from the perfect G graphene sheet to form the defects, and n is the number of Pd atoms adsorbed. z and v are the numbers of hydrogen molecules and atoms, respectively. μ_c is the perfect graphene per atom total energy, μ_N is a half of the total energy of the N_2 molecule in the gas phase, E_G is the perfect (pristine) graphene energy and $E_{GN_xV_y}$ is the N-doped G-graphene with y-vacancy system energy. E_{Pd_n}, E_{zH_2} and E_{Pd_nvH} are the energies of n-palladium, z-hydrogen molecules and v-hydrogen atoms with the n-palladium cluster, respectively. A general system energy $E_{(a+b)}$ implies the a system with the b system included. For example $E_{(GN_xV_y+Pd_n)}$ is the energy of the N-doped G-graphene with the y-vacancy system and the included n palladium atom cluster.

3. Results and discussion

3.1 N-Graphene defects

Optimisation for the different types of N-doped graphene molecules as substrates was performed and is presented in Fig. S1 (ESI†). The theoretical nitrogen content (from 4.1 to 9.7%) in our super-cell models was calculated. The experimental ones (where the substrate is made of pyridinic and graphitic type defects) synthesised *via* the deposition–precipitation method of ref. 36 were 5.7, 8.6 and 11.3%.

Parambhath synthesised N-doped graphene *via* nitrogen plasma treatment of hydrogen exfoliated graphene.[26] The nitrogen content was 7% with pyridinic, pyrrolic and graphitic type defects. In this sense, the super-cell model is comparable to some other experimental results. The calculated defect formation energies (pyrrolic and pyridinic defects), magnetic moment, formation energies with Pd atoms, adsorption energy with Pd, total charge, and magnetic moment with metal and nitrogen content are shown in Table 1 and Table S1 (ESI†).

The formation energies for some graphene defects are consistent with previous calculations.[38,49] Apparently the stability (in this case formation energy is used) of defect configuration is:

$\Delta E_f(N_3V_1) < \Delta E_f(N_2V_1) < \Delta E_f(N_1V_1)$ and

$\Delta E_f(N_4V_2) < \Delta E_f(N_3V_2) < \Delta E_f(N_2V_2) < \Delta E_f(N_1V_2)$ for pyridinic defect,

$\Delta E_f(N_3V_3) < \Delta E_f(N_2V_3) < \Delta E_f(N_1V_3)$ and

$\Delta E_f(N_3V_1) < \Delta E_f(N_1V_1)$ for pyrrolic defect.

Table 1 Formation energies (pyrrolic and pyridinic systems of Fig. 1) ΔE_f (eV), total magnetic moment m (μ_B), formation energies with Pd atoms $\Delta E_{f_{Pd}}$ (eV), adsorption energy with Pd $E_{ad_{Pd}}$ (eV), net charge Q_{Pd} (e), magnetic moment with metal m_{Pd} (μ_B) and nitrogen content N (%)

System	ΔE_f	m	$\Delta E_{f_{Pd}}$	$E_{ad_{Pd}}$	Q_{Pd}	m_{Pd}	N%
N_3V_3-pyrrolic	8.07	0.10	3.97	4.10	+0.8	0.00	6.41
N_3V_1-pyrrolic	5.52	0.92	2.84	2.68	+0.6	1.27	6.12
N_4V_2-pyridinic	3.65	0.00	−1.83	5.48	+0.9	0.00	8.33
N_3V_1-pyridinic	3.30	0.35	0.74	2.46	+0.6	1.13	9.67

It is important to mention that the N_2V_1 pyrrolic defect evolves into an N_2V_1 pyridinic defect (see the ESI,† Table S1 and Fig. S1).

The N_4V_2, N_1V_1 pyridinic and N_1V_1 pyrrolic defects are non-magnetic, while all other defects are spin-polarised. The most important magnetism and energetic behaviour of carbon–nitrogen defects in graphene is mainly related to carbon sites of low (two) coordination number, generated by introducing vacancies to a pristine graphene. The breakdown of spin symmetry and magnetism is observed in our projected density of state (PDOS) calculations. However, replacing these carbon sites with nitrogen sites decreases magnetism and produces energetically more favourable structures. In this way, the N-doped graphene is energetically more favourable when compared to the configuration of only a single vacancy or double vacancies in graphene. The formation energies of single, double and triple vacancies in graphene are 7.29, 7.05 and 10.08 eV (167.67, 162.58 and 232.45 kcal mol^{-1}), respectively (see the ESI†). These results are consistent with previous calculations.[48]

Our results show that nitrogen atoms may stabilize single, double and triple vacancy formation in graphene. Generally, it appears that the formation energy for N_xV_y decreases with the number of nitrogen atoms. These results suggest that the concentration of defects N_3V_1 and N_4V_2 pyridinic, and N_3V_3 and N_3V_1 pyrrolic, which are usually obtained under harsh conditions, will predominate more than other defects under experimental conditions.

3.2 Adsorption of one Pd atom on defects

In order to investigate the effect of N-doped defects, a metal Pd atom was added to the sheet and the new system was revealed (see Fig. 1).

The metal atom was adsorbed at different sites. In all cases, the most stable site was the one above the vacancy. The binding energy was up to four and half times higher than the binding energy of the Pd atom supported on graphene.[50,51] When a metal atom was absorbed by defects, the metal was bound to nitrogen atoms and a change in the molecular carbon–nitrogen bond length was observed. Table 1 lists the calculated formation energy and charge transfer of one palladium atom adsorbed on the N-doped graphene sheets. The lowest adsorption energies suggest that the Pd atom on defects acts as a nucleation site for clusters. For pyrrolic defects, our calculated results indicate that the palladium atom binds more strongly to the N_3V_3 defect than to the N_3V_1 one (see Table 1). Contrastingly in the case of the pyridinic system, the palladium atom binds

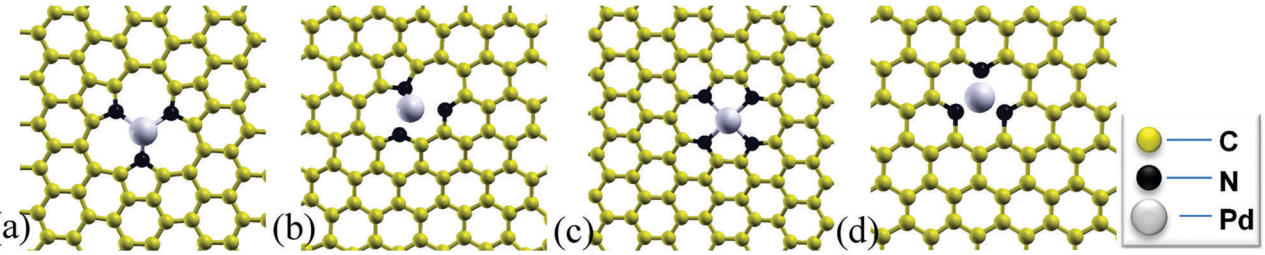

Fig. 1 Optimized stable structures of one palladium atom adsorbed on different substrates: in (a) N_3V_3 pyrrolic defect, (b) N_3V_1 pyrrolic substrate, (c) N_4V_2 pyridinic defect and (d) N_3V_1 pyridinic substrate. The colored circles in yellow, black and gray represent carbon, nitrogen and palladium atoms, respectively.

more strongly to the N_4V_2 defect than to the N_3V_1 defect. As it appears judicious to analyse all defects, the spill-over mechanism for the N_3V_3 pyrrolic defect will be studied and some results will be compared with the N_3V_1 pyridinic defect. Other defects will be dealt with in further study. In fact, we recently studied the first stage of the hydrogen spill-over mechanism for the N_3V_1 pyridinic defect.[29] A Löwdin population analysis revealed that electronic charge from Pd is transferred to the N-graphene system. Consequently, electronic charge fills acceptor like states (see Table 1). In contrast, Fig. S2 (ESI†) shows two surfaces (positive and negative) that manifest the constant electron-density difference ($\Delta\rho$) for N_3V_3 pyrrolic and N_3V_1 pyridinic defects and also show a small donation of electrons from Pd orbitals to N (see Section S2 in the ESI†).

3.3 Adsorption of Pd clusters on defects

Different isomer orientations and structures of Pd_n, n = 2, 3, 4 clusters were considered in this work. The adsorption energies of Pd_n clusters supported on the pyrrolic-nitrogen substrate are shown in Table 2.

3.3.1 Pd_2 cluster. Two different orientations (perpendicular and horizontal to the pyrrolic-nitrogen plane) were studied in this case. In the horizontal Pd_2 cluster orientation, one Pd atom was placed on a vacancy and the other one over a carbon atom (Fig. 2(a)). The binding energy was 0.86 eV (19.78 kcal mol^{-1}) bigger than the binding energy of vertical Pd_2 orientation, Fig. 2(b). The distance between two Pd atoms was 2.72 Å larger than the distance of free Pd_2 (2.52 Å[51]). Besides this, one Pd was bonded to the nitrogen and the other one to the nearest carbon atom (see Fig. 2(a)). The palladium magnetic moments were 1.13 (Pd on a vacancy) and 0.10 μ_B (Pd on carbon). Furthermore the values of the three nitrogen magnetic moments are 0.13, 0.21 and 0.17 μ_B. The Pd net positive-charge was +0.90 (on a vacancy) and +0.25 (on carbon). Notably, nitrogen atoms generally show a net negative charge of 0.35 per atom.

3.3.2 Pd_3 cluster. In the case of three palladium atoms, sloping triangular orientation was the most stable orientation, where one Pd was found on the vacancy and the other two on top of C atoms, Fig. 2(d). The Pd–Pd average distance was 2.67 Å, which was larger than the distance of free Pd_3 clusters. Likewise, N–Pd bond formation came from the interaction between N sp^2, p_z and Pd electron orbitals. The Pd net positive-charges of +0.82 (on a vacancy) and two of +0.16 (on carbon) were calculated. Similarly, nitrogen atoms presented a net negative charge of −0.34 per atom. The total magnetic moment was 1.74 μ_B. In contrast, Pd_3 sloping triangular orientation on the pyridinic defect had a magnetic moment of 1.00 μ_B.[29] The interaction between defects and metal clusters shown in these results may explain the role that defects play in the electronic properties of metallic clusters.

3.3.3 Pd_4 cluster. Pd_4 clusters represent interesting cases because Pd atoms nucleate into three-dimensional tetrahedral clusters, which are the smallest Pd clusters with a three dimensional structure. An inverted tetrahedron (see Fig. 2(f)) was the most stable configuration with magnetization 2.00 μ_B (2.80 μ_B for Pd_4 on pyridinic).[29] The Pd atom on the vacancy had a net positive charge of +0.75. Nitrogen atoms have a net negative charge of −0.31 per atom. It is important to mention that the Pd cluster adsorption energies on pyrrolic defects were up to three and half times higher than the Pd cluster adsorption energies on graphene[50] (see Table 2). Thus, we present local magnetic moments for Pd_2 (a), Pd_3 (c), and Pd_4 (f) clusters in Table S2 (ESI†) with labels corresponding to those in Fig. S5 (ESI†).

Table 2 Adsorption energies E_{ad} (eV) and E_{adG} (eV)[50] on pyrrolic defects and graphene, respectively, distances d_{Pd-N} (Å), and total pyrrolic-N magnetic moments m (μ_B) of Pd_n. Optimised structures of Fig. 2

n	Structure	E_{ad}	E_{adG}	d_{Pd-N}	m
2	Horizontal (a)	4.67	1.28	2.06	2.00
2	Vertical on vacancy (b)	3.81		2.08	3.00
3	Vertical triangular (c)	3.59	1.44	2.11	2.82
3	Sloping triangular (d)	4.06		2.08	1.74
3	Horizontal triangular (e)	3.67		2.07	2.00
4	Inverted tetrahedron (f)	3.84	1.80	2.10	2.00
4	Tetrahedron aligned (g)	2.54		2.16	3.00
4	Horizontal rhombus (h)	3.23	1.55	2.14	3.20

3.4 Hydrogen interaction with Pd clusters supported on the pyrrolic substrate

3.4.1 Pd atom. We studied the interaction between hydrogen atoms and the substrate, together with the catalyst. The former interactions explore the capacity to adsorb hydrogen atoms. In the N_3V_3 pyrrolic system, adsorption of two hydrogen molecules was investigated. If the catalyst comprises one Pd atom the saturated system was formed from one hydrogen molecule (Fig. 3(a))

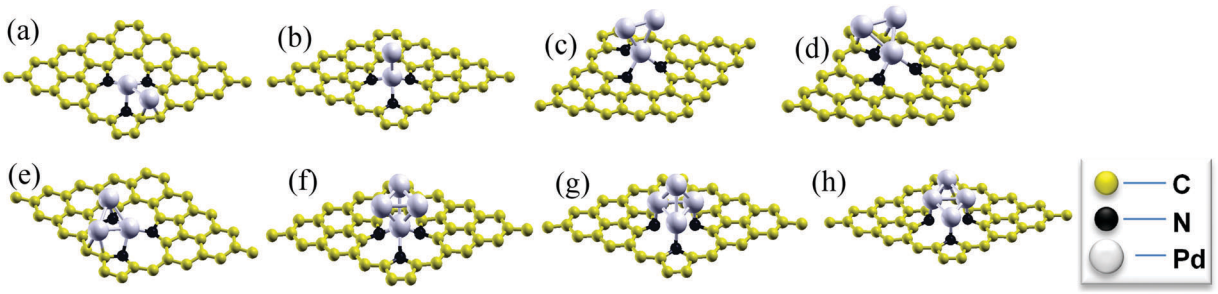

Fig. 2 Optimized structures of different Pd_n clusters supported on the N_3V_3 pyrrolic substrate. In (a) horizontal and (b) vertical Pd_2 structures; (c)–(e) triangular Pd_3 structures. (f)–(h) Pd_4 clusters. The colored circles in yellow, black and gray represent carbon, nitrogen and palladium atoms, respectively.

favoured by charge exchange. The hydrogen molecule adsorption energy is 0.77 eV (17.71 kcal mol^{-1}). In contrast, if the pyridinic N_3V_1 substrate is analysed, the saturated system is formed from two hydrogen molecules with energies of 1.20 and 0.90 eV per H_2.[29] Furthermore, NEB showed molecular activation without a barrier. We calculated distances of 1.91 Å (Pd–H) and 0.80 Å (H–H) for the pyrrolic substrate. The C–N bonds remained unchanged and the metal–N bond grew slightly. Electronic transference, known as back donation,[52] from the occupied metal d orbitals to the anti-bonding (σ*) state of H_2, was observed following hydrogen adsorption.

However, it appears that electronic charge from the (σ) bonding state of H_2 is transferred to the unoccupied Pd. The total magnetic moment in this system is 2.00 μ_B. In this case,

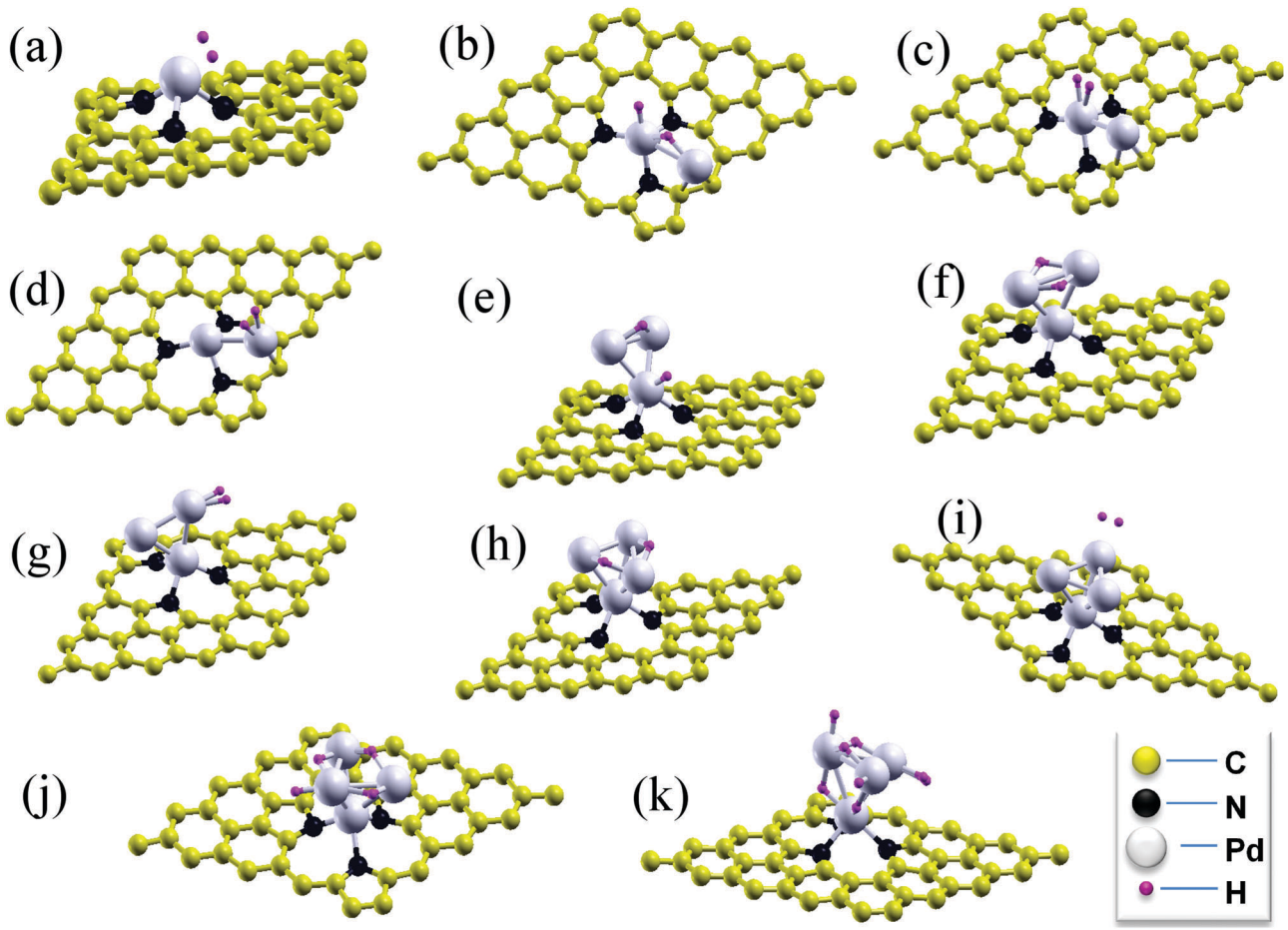

Fig. 3 Adsorption of hydrogen molecules around the Pd clusters anchored onto the N_3V_3 pyrrolic defect. (a) Activated state of the H_2 molecule adsorbed on the Pd atom. (b) Dissociated state of the H_2 molecule, and (c) and (d) activated states of the H_2 molecule adsorbed on Pd_2 clusters. (e and f) Dissociated states of the H_2 molecule on Pd_3 and (g) activated state of the H_2 molecule adsorbed on Pd_3. (h, j and k) Dissociated states of H_2, $2H_2$ and $3H_2$ molecules on Pd_4, respectively, and (i) activated state of the H_2 molecule adsorbed on the Pd_4 cluster. The colored circles in yellow, black, gray and purple represent carbon, nitrogen, palladium and hydrogen atoms, respectively.

contributions from the most localised non-bonding d-orbitals determine the spin configuration and the magnetic moment. In fact, Pd has a net positive charge of +0.90. The adsorption energy for the $Pd(H_2)$ complex on the vacancy was 3.97 eV (91.31 kcal mol^{-1}). This value was five times higher than the binding energy of H_2 (0.77 eV) on Pd over the vacancy, and desorption of these complexes did not compete with desorption of one hydrogen molecule from the adsorbed Pd. Therefore this mechanism does not limit the reversibility of hydrogen desorption.

3.4.2 Pd_2 cluster. The interaction of H_2 with Pd_2 clusters on pyrrolic defects was also studied. One H_2 molecule interaction with the system generated two active states (Fig. 3(c) and (d)) and one dissociated state (Fig. 3(b)). Our results are presented in Table 3. From the NEB calculation, it was found that two molecular activations occurred without a barrier. In both cases, a H_2 molecule was placed on top of each Pd atom. The stability gained by the Pd_2H_2 complex due to the adsorption of one hydrogen molecule is substantial (see Table 3). For active states, H_2 adsorption reduces the magnetic moment of the Pd_2 cluster. Next, the NEB method was employed to determine the reaction path for the dissociated case, beginning with the active one (see Fig. 3(c)). The barrier energy for the dissociated state H_2 was small (Table 3). This means that the process can occur spontaneously at room temperature. The adsorption energy for the $Pd_2(H_2)$ complex on the vacancy was 4.52 eV (103.96 kcal mol^{-1}). This value was eight times higher than the binding energy of H_2 on the Pd_2 cluster supported on pyrrolic defects. Apparently, desorption of complexes did not compete with desorption of one hydrogen molecule from the adsorbed Pd. Even so, an H–H bond length of 1.94 Å was found.

3.4.3 Pd_3 cluster. In this system, one activated state (see Fig. 3(g)) and two dissociated states were generated and are shown in Fig. 3(e) and (f). In both dissociated states, the adsorption energies were 1.18 and 1.49 eV per H_2, respectively. Again, the NEB method was employed to determine the reaction path for the dissociated case starting from the active one (Fig. 3(g)). In comparison, a dissociated binding energy of 1.28 eV (29.44 kcal mol^{-1}) was found in the pyridinic (N_3V_1) system.[29] For the case of the hydrogen activated state, the Pd–H distance was 1.70 Å and the H–H bond distance was 0.871 Å. The Pd_3 cluster anchored onto pyrrolic defects appears to bind only one hydrogen molecule in the dissociated state. As apparent in Fig. 3(e) and (f), the orientation of Pd_3 became slightly bent when H_2 was adsorbed. Likewise, a NEB calculation revealed that molecular activation occurred without a barrier. Cabria *et al.*[51] found an activated binding energy (in the case of Pd_3 supported on graphene) of 0.51 eV (11.73 kcal mol^{-1}), similar to our result. In the case of Fig. 3(e), the process may have occurred spontaneously at room temperature, when the H–H bond length was 2.46 Å. In contrast, Cabria found that there was no energy barrier[51] for all the dissociated states of a H_2 molecule in Pd_3 supported on graphene. They also found a zero magnetic moment for both the active and dissociated states, similar to Pd and Pd_2 on graphene.[51]

3.4.4 Pd_4 cluster. H_2 molecule interaction with the most stable configuration of Pd_4 tetrahedron (see Table 3) leads to two types of hydrogen adsorption states. The first one is an activated H_2 state with no barriers where the H–H bond length is relaxed, Fig. 3(i). Several Pd–H (1.90 Å) and H–H (0.80 Å) distances were found. The C–N bonds remained unchanged. The second state is a hydrogen dissociated state (Fig. 3(h), (j) and (k)). In order to study the first H_2 molecule dissociation (Fig. 3(h)), we started from the active state (Fig. 3(i)). Analogously in the cases of Fig. 3(j) and (k), the initial states for reaction paths were active states of H_2 molecules located on top of the Pd atoms. The hydrogen saturation of the Pd_4 cluster plays a central role in the study of hydrogen migration from the catalyst to the substrate. We found that when hydrogen molecules interact with the Pd_4 cluster supported on pyrrolic-graphene, three of these bind in dissociated states and the other binds in the activated H_2 state with no barriers (see Fig. 3(k)). The five remaining H_2 molecules did not bind directly to the Pd cluster and remained practically unaltered with respect to isolated H_2. These results can be compared with previous calculations where the saturation of the Pd_4 cluster occurs with four hydrogen molecules in active states.[31] In our case, the adsorption of multiple H_2 molecules dramatically deformed the tetrahedral geometry of the Pd_4 cluster.

The average Pd–Pd bond distance for the $Pd_4 6H–H_2$ complex was 2.85 Å, which was longer than that for the Pd_4 cluster anchored onto pyrrolic defects (2.59 Å). We found a strong influence on the hydrogen–metal interaction caused by the hybridisation between the pyrrolic defect and the Pd atoms.

Table 3 The ($Pd_nz(H_2)$) complex of Fig. 3, energy adsorption complex (eV), gain stability complex (eV), energy adsorption of hydrogen (eV), dissociated barrier energy (eV) and magnetic moment (μ_B)

System	Energy adsorption complex	Gain stability	Energy adsorption of H_2	Barrier energy for dissociated state H_2	Magnetic moment
PdH_2 (a)	3.97	−0.13	0.77	0	2.00
$Pd_2$2H (b)	4.52	−0.15	1.12	0.34	1.44
Pd_2H_2 (c)	4.71	0.04	0.43	0	1.60
Pd_2H_2 (d)	5.20	0.53	0.92	0	2.00
$Pd_3$2H (e)	4.12	0.53	1.18	0.41	0.24
$Pd_3$2H (f)	4.23	0.64	1.49	1.23	1.80
Pd_3H_2 (g)	3.71	0.12	0.60	0	1.80
$Pd_4$2H (h)	4.21	0.37	1.34	0.61	2.15
$Pd_4(H_2)$ (i)	3.60	−0.24	0.22	0	0.55
Pd_4(4H) (j)	4.20	0.35	1.25	0.62	0.00
$Pd_4(6H–H_2)$ (k)	4.16	0.32	1.12	0.64	0.00

The energy barriers for dissociated states were below 0.64 eV (14.49 kcal mol^{-1}) (Table 3). This means that the process may occur spontaneously at room temperature. As expected, the number of adsorbed H_2 molecules increased with the particle size. Table 3 presents the changes in the adsorption energies of H_2 with the number of adsorbed H_2 molecules on the Pd_4 anchored on pyrrolic defects. It was found that the first H_2 dissociates from the Pd_4 cluster forming a hydride with a larger binding energy of 1.33 eV (30.59 kcal mol^{-1}). This large energy shows a strong chemisorptive interaction. The second molecule is adsorbed with energies of 1.24 eV (28.52 kcal mol^{-1}) and 1.12 eV (25.76 kcal mol^{-1}) for the third molecule, respectively (Table 3). In the case of the Pd_4 cluster anchored on the pyridinic (N_3V_1) defect, saturation was found to occur after adsorbing only two H_2 molecules in dissociated states. In this way, defects of graphene play an important role in modulating hydrogen adsorption. Our calculations show a gain in stability for the Pd_nvH complexes on the pyrrolic defect, indicating that the anchoring avoids the migration of the Pd_nvH complex on the surface, a problem that diminishes the hydrogen storage capacity of the material.

3.5 Hydrogen migration from the Pd cluster onto the supporting N-doped graphene substrate

Hydrogen migration from the catalyst to the substrate is the most important stage in the hydrogen spill-over mechanism. Thus, we used and studied pyridinic N_3V_1 and pyrrolic N_3V_3 substrates together with the catalyst Pd_n (n = 3, 4) to explore capacity for hydrogen storage. For a sufficiently high H_2 pressure, the surfaces of the catalyst particles are fully covered by H atoms in the saturated state. Hydrogen molecules dissociated and ready to migrate, as shown in Fig. 3(e), (h), (j) and (k), represented the initial stage of our migration calculations. After geometry optimisation, initial (i) and final (iii) states were obtained and are presented in Fig. 4–6. Transition states (ii) were also observed in the same former figures by using NEB and analysed by applying vibrational frequency calculations. For clarity, red circles and arrows were drawn in transition states; see Fig. 4–6, for the hydrogen migration direction, pointing to the closest and unoccupied C atom on the substrate. It is important to mention that migration energy barriers must be low enough to achieve fast kinetics at room temperature. Furthermore, hydrogen migration barrier energies were estimated with constrained geometry optimisation by gradually changing the Pd–H bond distance.

Along these lines, for the catalyst Pd_3, migration energy barriers around 2.09 eV (pyridinic defect) and 1.59 eV (pyrrolic defect) (48.19 and 36.67 kcal mol^{-1}, respectively) were found, Fig. 4. In the same way, buckling on the surface was observed as a consequence of the chemisorbed hydrogen.

For catalyst Pd_4, a Pd–H distance of 1.60 Å (on pyrrolic defect) and 2.09 Å (on pyridinic defect) was calculated in the transition state (ii) of Fig. 5. We also found several migration energy barriers of 1.99 eV (45.89 kcal mol^{-1}) on pyrrolic defects and 1.64 eV (37.81 kcal mol^{-1}) on pyridinic defects. As apparent in the former figure, migration reaction is actually an endothermic process and hydrogen migration is curtailed under ambient conditions.

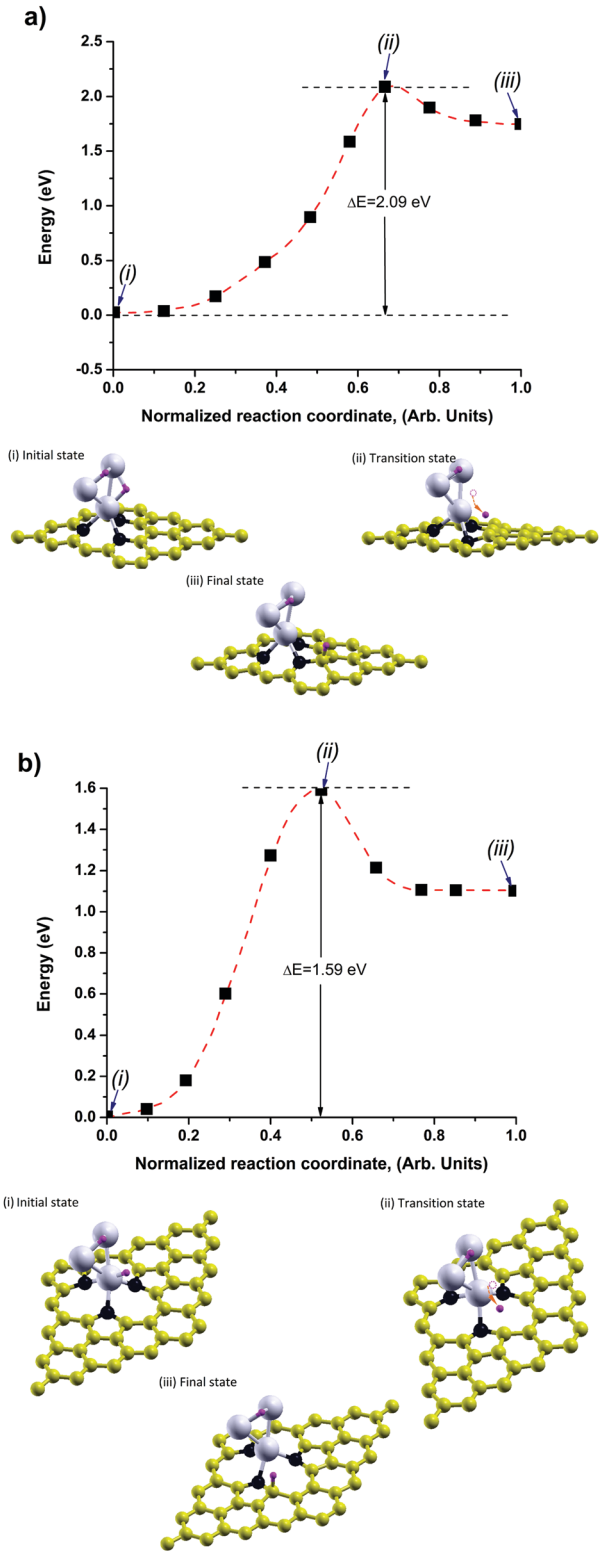

Fig. 4 Reaction path states (black squares) of the hydrogen migration process. The hydrogen migration process follows the trajectory of the Pd_3 cluster to different substrates. Normalized reaction coordinate (in arbitrary (Arb) units) *vs.* energy (in eV) can be observed. Optimized structures of initial (i), transition (ii), and final (iii) states are also included. In (a) is presented the migration to the saturated N_3V_1 pyridinic substrate and in (b) that to the N_3V_3 pyrrolic one. The colored circles are the same as in Fig. 3. The red dashed line is a guide for the eye. The details are given in the text.

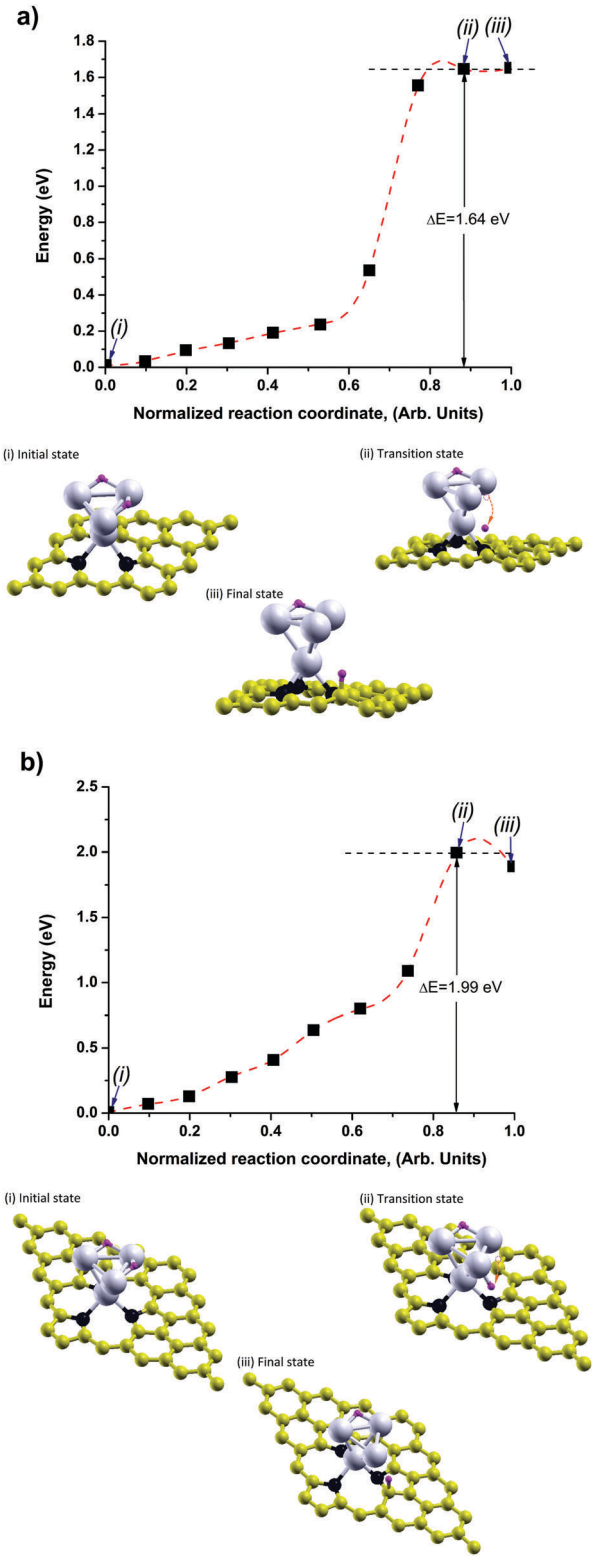

Fig. 5 Reaction path states (black squares) of the hydrogen migration process are presented. The hydrogen migration process follows the trajectory of the Pd_4 cluster to different substrates. Normalized reaction coordinate (in arbitrary (Arb) units) *vs.* energy (in eV) can be observed. Optimized structures of initial (i), transition (ii), and final (iii) states are also included. In (a) is presented the migration to the N_3V_1 pyridinic substrate and in (b) that to the N_3V_3 pyrrolic one. The colored circles are the same as in Fig. 3. The red dashed line is a guide for the eye. The details are given in the text.

Likewise, buckling on the surface and a C–N bond length change, from 1.34 Å to 1.45 Å, were observed, see Fig. 5. In contrast, the C atom is a favourable site for adsorbing hydrogen, reflected by the adsorption energy calculated to be $E = 1.08$ eV (24.84 kcal mol^{-1}). Notably, other authors[53] obtained values of around 0.86 and 1.68 eV (19.78 and 38.64 kcal mol^{-1}, respectively).

The substrate has a very important effect on hydrogen migration. N-Doping not only enhances the H adsorption strength of the substrate but also leads to general weakening of the H chemisorption strength on the saturated Pd_4 cluster. This eventually results in a thermodynamically improved migration reaction, accompanied by a substantial fall in migration barrier energy for the saturated Pd_4 cluster on pyrrolic (1.34 eV = 30.90 kcal mol^{-1}) and pyridinic defects (0.84 eV = 19.37 kcal mol^{-1}) as displayed in Fig. 6(a) and (b). Similarly, a C–H bond distance of 1.13 Å was calculated in the former pyrrolic defect. In our calculations, an intermediate migration stage is observed in the saturated Pd_4 cluster on the pyrrolic defect, Fig. 6(c).

The corresponding migration barrier energy is 0.50 eV. The HSE hybrid functional was only used to recalculate single-points in the reaction paths (Fig. 4–6). The adsorption energy thresholds of the complexes (on pyridinic and pyrrolic defects) do not vary significantly between GGA (PBE) and HSE hybrid functionals (below 0.19). The difference between these values is not very large, validating the application of PBE to this system. In contrast, in the case of hydrogen migration, a difference was found (below 0.2 eV, see Table S3, ESI†) between the barrier energy values calculated with PBE and HSE. This means that GGA (PBE) and HSE hybrid functionals thus predict hydrogen migration from the catalyst to the substrate at room or moderate temperature. The energies of the product are shown to be higher than those of the reactant. Therefore, migration processes are endothermic reactions with a positive change in enthalpy ($\Delta H > 0$) and an increase in entropy ($\Delta S > 0$). For this reason, the most probable reaction pathway is the migration to the substrate in this temperature range. This behaviour is consistent with accessible states on the catalyst metallic surface. Thus, if we have enough energy, Gibbs free energy can become negative, so that the reaction will go smoothly and efficiently. Likewise, we calculated an electronic charge transference of 0.32 e (from the hydrogen migrated atom to the substrate). In this case, hydrogen migration can be statistically modelled using the Arrhenius law.

$$\nu_{\mathrm{migr}} = \nu_0 \exp\left[\frac{-\Delta E}{k_{\mathrm{B}} T}\right] \tag{6}$$

Here, the migration rate at a given temperature is determined using the migration barrier (ΔE, see Fig. 4–6) and the attempt frequency (k_{B} is the Boltzmann constant). In the following, room temperature and an attempted frequency of ν_{migr} will be used to model our systems. The ν_{migr} (eqn (6)) value is motivated by the estimate of the phonon frequency of $\nu_0 = \frac{k_{\mathrm{B}} T}{h} = 6.00 \times 10^{12}$ s^{-1}.

Assuming maximum (0.10 s^{-1}) and minimum (1.00×10^{-6} s^{-1}) observable hopping frequencies, migration barrier energies may be accessible in Atomic-Force Microscopy AFM experiments.

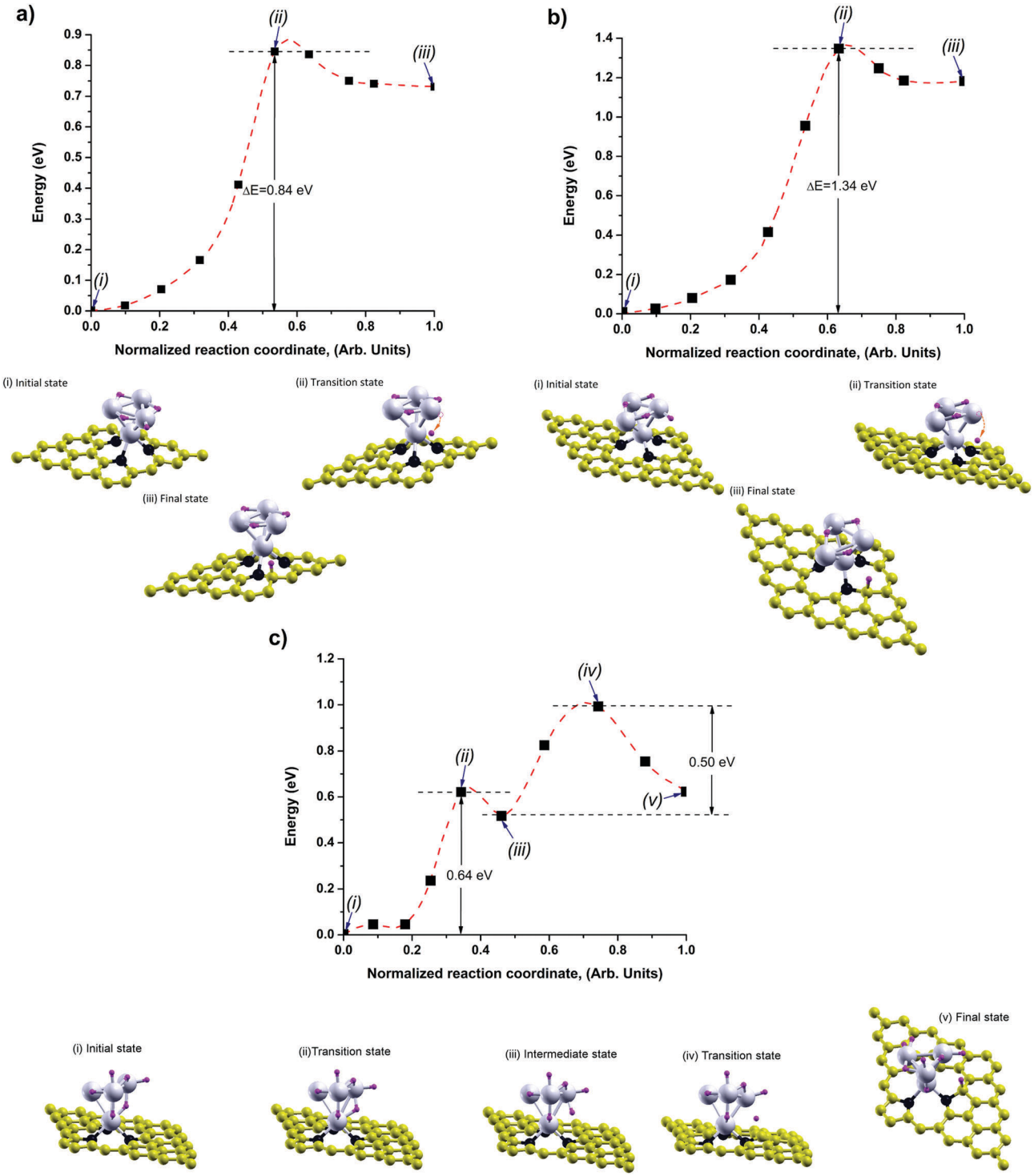

Fig. 6 Reaction paths of the hydrogen migration process. The hydrogen migration process follows the trajectory of the Pd_4 cluster (with different quantities of hydrogen) to different substrates. Normalized reaction coordinate (in arbitrary (Arb) units) *vs.* energy (in eV) can be observed. Optimized structures of initial (i), transition (ii), and final (iii) states are also included. In (a) is presented the migration from the Pd_4 cluster with 4 hydrogens to the saturated N_3V_1 pyridinic substrate, in (b) the migration from the Pd_4 cluster with 4 hydrogens to the N_3V_3 pyrrolic substrate and in (c) the migration from the Pd_4 cluster with 8 hydrogens to the N_3V_3 pyrrolic substrate. In this case an initial (i), two transition (ii) and (iv), one intermediate (iii) and a final (v) states are presented. The colored circles are the same as in Fig. 3. The red dashed line is a guide for the eye. The details are given in the text.

Migration barrier energies as a function of temperature can be observed in Fig. 7. It is concluded that for observable hopping frequencies under room temperature conditions, a feasible process presents migration barrier energies between 0.7 and 1.1 eV or lower, *i.e.* the pyridinic N_3V_1 defect system or pyrrolic N_3V_3 defect, see Fig. 6(a) and (c).

Applying the Arrhenius law in this work revealed high hopping hydrogen migration frequencies. This model is shown in Fig. 8 where isotherms and migration frequencies as a function of migration barrier energy are presented, for minimum hopping frequency (1×10^{-6} s^{-1}) and maximum observable hopping (0.1 s^{-1}). Consequently, a massive migration process is observed (Fig. 8).

These frequencies occur in the range of seconds for saturated Pd clusters decorated with pyrrolic defects. In the case of oversaturated Pd clusters, the migration process is apparent in the range of milliseconds. Following this argument, the spill-over process is characterized experimentally by a high density of pyridinic and pyrrolic defects, but is dependent on manufacturing conditions, resulting in a great capacity for hydrogen storage.

According to our theoretical results the migration barrier energies are small enough for this process to be highly probable at room temperature. Similarly experimental evidence shows that the migration process of hydrogen from the catalyst (Pd nanoparticles, 3.1 nm) to the substrate (pyrrolic or pyridinic defects) can be massive, although this is dependent on manufacturing conditions. Contrastingly, the experimental results exhibit significantly a small uptake capacity increase of hydrogen (below of 0.07%) when the graphene is decorated with palladium[26] (see Section S3 in the ESI†). This could be attributed only to the presence of micro-pores in the graphene sheets and also indicates the inefficient hydrogen adsorption by the Pd particle agglomerates (sized of 50 nm).[26] Notably, other authors recently applied density functional theory to study the hydrogen spill-over mechanism on Pd_6 and Pd_{13} clusters, supported on graphene.[25] They have not found a single case of H atoms or H_2 molecules spilling over the carbon substrate.[25] These results suggest that the migration of hydrogen from the catalyst (Pd cluster or nanoparticle) to the graphene is thermodynamically and kinetically very difficult.

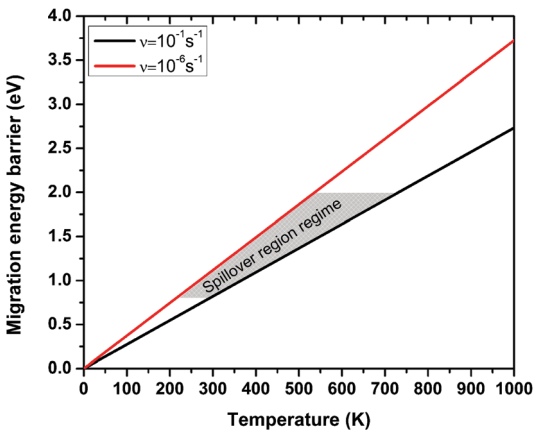

Fig. 7 According to the Arrhenius law (eqn (6)) hydrogen migration energy barriers (ΔE) as a function of temperature for two observable hopping frequencies of 0.1 s^{-1} (maximum) and 1×10^{-6} (minimum) are given. The shadow area corresponds to a particular spill-over region regime.

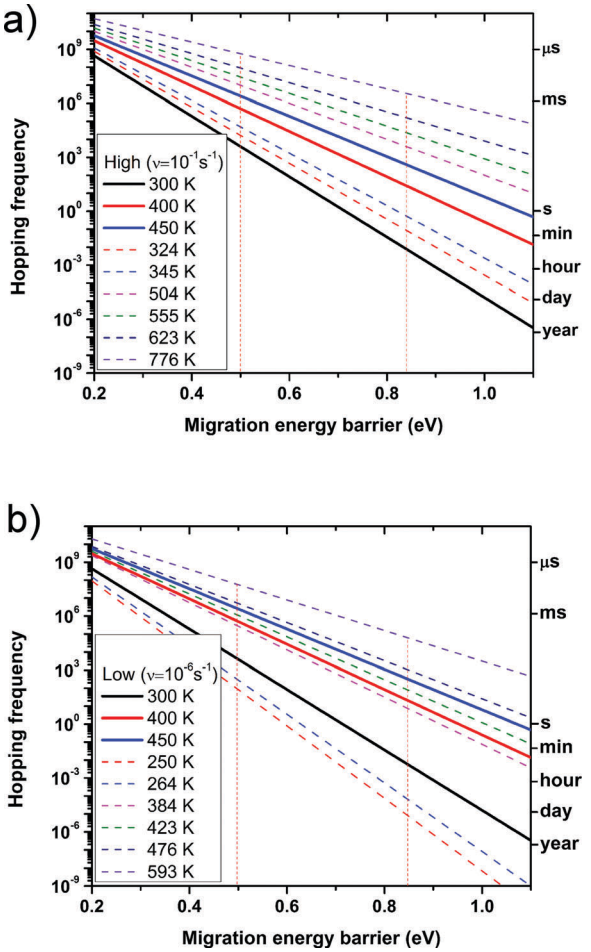

Fig. 8 Hopping frequency for different migration energy barriers (normalized to 1000 hops) and temperatures. Two observable hopping frequencies of 0.1 s^{-1} (maximum) (a) and 1×10^{-6} (minimum) (b) were considered. Vertical dashed lines are two representative migration energy barriers in our systems. The high probability of massive migration was found in time ranges around a few seconds.

3.6 Diffusion of hydrogen on the supporting N-doped graphene substrate

Hydrogen atom diffusion pathways (on substrate) were studied using the nudged elastic band (NEB) method. For convenience, the saturated Pd_3-2H cluster supported on the N_3V_3 pyridinic substrate was used and the super-cell can be observed in Fig. 9. The former cluster was presented because similar diffusion results were obtained for other systems studied (systems represented in Fig. 4–6). Our initial diffusion step, the equilibrium state located at the A carbon atom of Fig. 9, is the final state of the hydrogen migration process previously studied *i.e.* from the saturated Pd_3-2H cluster to the substrate (see Fig. 4(a)). Four possible diffusion pathways, from the initial state to carbon atoms 1, 2 and 3 and desorption, were studied. Pathways 1 and 2 behave in a similar way with a migration energy barrier of approximately 0.8 eV (18.4 kcal mol^{-1}) in both cases, Fig. 9. The most important difference is the exo(endo) thermic character of the 1 (2) final state, respectively, Fig. 9. Besides this, we calculated a diffusion energy barrier of 3.28 eV for pathway 3 (not shown in Fig. 9).

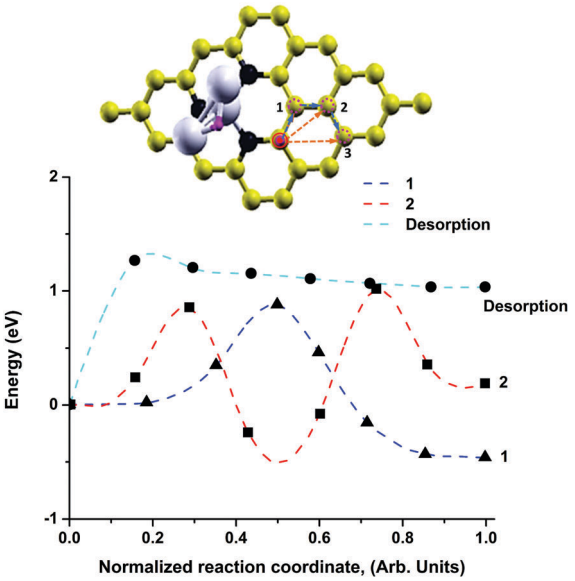

Fig. 9 Diffusion barriers for different paths of single hydrogen migration as a function of the normalized reaction coordinate. Arrows indicate different carbon to carbon diffusion pathways as follows: 1: CA → C1 in blue, 2: CA → C1 → C2 in red, and 3: CA → C3 in orange, for this particular trajectory a diffusion energy barrier of 3.28 eV was calculated. It is concluded that this diffusion cannot occur at room or moderate temperatures. This is the reason why this trajectory is not shown in the figure. Finally desorption represents the hydrogen atom movement away from, in the normal direction, its surface.

We concluded that this diffusion cannot occur at room or moderate temperatures. In the same way in Fig. 9, a carbon atom in position 2 was substituted by a nitrogen atom (a graphitic-like defect) and the diffusion process between carbon atom 1 and the former nitrogen was studied. A diffusion barrier energy of 2 eV was found. In this way, a graphitic-like diffusion cannot occur at room temperature. Contrastingly, the desorption pathway represents the hydrogen atom movement away from its surface, in the normal direction.

A hydrogen atomic desorption energy barrier of 1.25 eV (28.75 kcal mol^{-1}) (see Fig. 9) was found. In this case, the former energy barrier is ~0.46 eV (10.58 kcal mol^{-1}) lower than the hydrogen thermal desorption energy. Besides, the chemisorbed hydrogen diffusion on the substrate is not limited by the thermal desorption of H. In contrast, Borodin *et al.*[53] found that hydrogen transport on graphene involves strong competition between diffusion and detrapping. The static hydrogen detrapping barrier was 1.1 eV (25.3 kcal mol^{-1}) and the energy barrier for hydrogen diffusion was 1.0 eV (23 kcal mol^{-1}).[53] Finally, according to our results the chemisorbed hydrogen induces buckling on the surface, creating a local region with an effective compressive stress and producing an energetic cost derived from this deformation.

This energetic cost is shown in the adsorption/desorption pathway (Fig. 9) with a barrier energy of 0.25 eV. This barrier is similar for chemisorbed hydrogen on graphene.[8] MacKay found that this stress increases the barrier diffusion for H on graphene. This effect helps to form hydrogen nanoislands.[8] In this way, the adsorption of H on the substrate may take two forms: chemisorption of atomic hydrogen and chemisorption of small clusters of atomic hydrogen which may change the diffusion and detrapping of H.

4. Conclusions

In this work, we investigated individual stages for hydrogen storage *via* the spill-over mechanism on small palladium clusters supported on pyridinic and pyrrolic nitrogen doped graphene. Due to computational limitations, the present study only deals with small Pd clusters at the subnanoscale. Of course the small cluster model is a gross simplification of the realistic size of catalyst particles and does not resemble the catalyst particles used in practice. However, the cluster model possesses sharp corners, edges and kinks, which are often found to be the most active catalytic sites in the nanoparticles of experimental systems. Likewise, this model allows us to investigate the effects of full coverage of chemisorbed hydrogen on catalytic activities. Pyridinic and pyrrolic defects are an excellent platform for studying the doping effects, electronic structures, and chemical or even physical properties of N-graphene systems. Researchers have also recently synthesised Pd nanoparticles on nitrogen-doped graphene. It is also apparent that using appropriate nitrogen atoms, single (V_1), double (V_2) and triple (V_3) vacancies in graphene can be stabilized and formation energy decreases. These results suggest that the concentration of N_3V_1 and N_4V_2 pyridinic, and N_3V_3 and N_3V_1 pyrrolic defects, which are usually obtained under harsh conditions, will exceed other defects under experimental conditions. It was subsequently observed that Pd clusters are strongly bonded onto N doped vacancies during the decoration process. This indicates that pyridinic and pyrrolic vacancies act as nucleation sites for Pd clusters. Similarly, charge transfer and strong binding between the substrate and the palladium clusters (up to three and half times higher than the binding energy of the Pd cluster supported on graphene) prevented detachment and the coalescence of clusters and led to dissociated states of H_2. A strong influence on the hydrogen–metal interaction caused by the hybridization between pyrrolic or pyridinic defects and the Pd atoms was apparent. In dissociated cases of H_2 on Pd clusters, barriers below 0.6 eV (13.8 kcal mol^{-1}) were calculated. When the Pd_4 cluster is at full saturation of hydrogen, it was found that the dissociated H atoms on the Pd_4 cluster supported on pyridinic and pyrrolic defects have a barrier of 0.8 and 0.5 eV (18.4 and 11.5 kcal mol^{-1}), respectively, against migration from the catalyst to the substrate (calculations made by means of general gradient approximation, GGA). Additionally, the HSE06 hybrid functional was used to recalculate only single-points in the reaction paths for hydrogen migration. We found a difference of less than 0.2 eV, between the barrier energy values calculated with GGA and HSE06. We also observed that the energies of the product are higher than those of the reactant. This means that migration processes represent an endothermic reaction with a change in positive enthalpy and an increase in entropy. Thus, if sufficient energy is available, Gibbs free energy can become

negative and the reaction will proceed smoothly and efficiently. This means that hydrogen dissociation and migration may occur spontaneously at room or moderate temperature. Additionally, Pd_nvH complexes gain stability when they are put on the substrate, indicating that the anchoring prohibits the hydrogen migration of the Pd_nvH complex to the surface, a problem that diminishes the hydrogen storage capacity of the material. These results show that the interaction between the defects and metal particles may explain the role that defects play in the hydrogen migration from the catalyst to the substrate. By applying our Arrhenius law calculations, we found high hopping hydrogen migration (from catalyst to substrate) frequencies, with prowling times of milliseconds. The former indicates that hydrogen migration is massive. It also became apparent that chemisorbed hydrogen diffusion on the substrate is not limited by thermal desorption. In this case, the energy barrier for hydrogen diffusion was $\sim$0.46 eV (10.58 kcal mol^{-1}) lower than the energy of hydrogen thermal desorption. In contrast, evidence suggests that hydrogen transport on graphene involves strong competition between diffusion and detrapping. Our results indicate that chemisorbed hydrogen induces buckling on the substrate, creating a local region with an effective compressive stress. This stress may increase the barrier diffusion of H. This effect may help in forming hydrogen nanoislands. Thus, for small and big Pd clusters we believe that charge transfer and electron deficiency will qualitatively play the same role (in the spill-over mechanism) when they are placed on the substrate. In contrast local and other effects (due to the size of the clusters) that eventually lead to quantitative changes in the height of dissociation/migration barriers will be a matter of further study. Our results for small clusters and experimental evidence for nanoparticles[26] suggest that the heights of the dissociation/migration hydrogen barriers are below 0.8 eV. This means that the hydrogen spillover mechanism might occur spontaneously at room temperature.

Finally, the importance of results obtained in this work refers to the development of experimental strategies which will enhance hydrogen storage using the spill-over mechanism. The best system for enhancing the hydrogen migration mechanism from the catalyst metal onto the substrate appears to involve a Pd_4 cluster supported on pyrrolic defects transferred onto graphene. Likewise, in order to stimulate a highly efficient diffusion mechanism of chemisorbed hydrogen, a substrate with free or low density of graphitic defects should be used.

Acknowledgements

We would like to thank the DGTIC-UNAM supercomputing centre for use of their facilities and technical assistance. We also acknowledge financial support from PRODEP, grants E. R. UAEH-PTC-715 DSA/103.5/15/7001, E. V. UAEH-PTC-723 DSA/103.5/15/10450, and Hernández-Hernández UAEH-PTC-693 DSA/103.5/15/7001. López-Pérez, P. A. is grateful for the support of "Apoyo a la Incorporación de Nuevos PTC 2015, F-PROMEP-39/Rev-04, DSA/103.5/15/7001". The authors would like to thank Citlalli Rios for her contribution in reviewing the grammar and style of the text.

References

1 Y. Miura, H. Kasai, W. A. Diño and T. Sugimoto, *J. Phys. Soc. Jpn.*, 2003, **72**, 995–997.
2 J. S. Arellano, L. M. Molina, A. Rubio and J. A. Alonso, *J. Chem. Phys.*, 2000, **112**, 8114–8119.
3 Y. Okamoto and Y. Miyamoto, *J. Phys. Chem. B*, 2001, **105**, 3470–3474.
4 M. Lai-Peng, W. Zhong-Shuai, J. Li, W. Er-Dong, R. Wen-Cai and C. Hui-Ming, *Int. J. Hydrogen Energy*, 2009, **34**, 2329–2332.
5 G. Srinivas, Y. Zhu, R. Piner, N. Skipper, M. Ellerby and R. Ruoff, *Carbon*, 2010, **48**, 630–635.
6 DOE Hydrogen program, annual program report. U.S. Department of Energy, 2006.
7 S. Casolo, O. M. Løvvik, R. Martinazzo and G. F. Tantardini, *J. Chem. Phys.*, 2009, **130**, 054704.
8 H. McKay, D. J. Wales, S. J. Jenkins, J. A. Verges and P. L. de Andres, *Phys. Rev. B: Condens. Matter Mater. Phys.*, 2010, **81**, 075425.
9 D. C. Elias, R. R. Nair, T. M. G. Mohiuddin, S. V. Morozov, P. Blake and M. P. Halsall, *Science*, 2009, **323**, 610–613.
10 P. Koskinen, S. Malola and H. Häkkinen, *Phys. Rev. Lett.*, 2008, **101**, 115502.
11 K. S. Subrahmanyam, P. Kumar, U. Maitra, A. Govindaraj, K. P. S. S. Hembram, U. V. Waghmare and C. N. R. Rao, *Proc. Natl. Acad. Sci. U. S. A.*, 2011, **108**, 2674–2677.
12 W. C. Connera and J. L. Falconer, *Chem. Rev.*, 1995, **95**, 759–788.
13 A. Lueking and R. T. Yang, *AIChE J.*, 2003, **49**, 1556–1568.
14 M. Marellaa and M. Tomaselli, *Carbon*, 2006, **44**, 1404–1413.
15 Y. Li and R. T. Yang, *J. Am. Chem. Soc.*, 2006, **128**, 8136–8137.
16 Y. Li and R. T. Yang, *J. Am. Chem. Soc.*, 2006, **128**, 726–727.
17 C. H. Chen and C. C. Huang, *Int. J. Hydrogen Energy*, 2007, **32**, 237–246.
18 C. H. Chen and C. C. Huang, *Microporous Mesoporous Mater.*, 2008, **109**, 549–559.
19 Y. Y. Liu, J. L. Zeng, J. Zhang, F. Xu and L. X. Sun, *Int. J. Hydrogen Energy*, 2007, **32**, 4005–4010.
20 R. Zacharia, S. Rather, S. W. Hwang and K. S. Nahm, *Chem. Phys. Lett.*, 2007, **434**, 286–291.
21 M. Zieliński, R. Wojcieszak, S. Monteverdi, M. Mercy and M. M. Bettahar, *Int. J. Hydrogen Energy*, 2007, **32**, 1024–1032.
22 R. Bhowmick, S. Rajasekaran, D. Friebel, C. Beasley, L. Jiao, H. Ogasawara and H. Dai, *J. Am. Chem. Soc.*, 2011, **133**, 5580–5586.
23 H. Y. Wu, X. Fan, J. L. Kuo and W. Q. Deng, *J. Phys. Chem. C*, 2011, **115**, 9241–9249.
24 G. M. Psofogiannakis and G. E. Froudakis, *J. Phys. Chem. C*, 2009, **113**, 14908–14915.
25 M. Blanco-Rey, J. I. Juaristi, M. Alducin, M. J. López and J. A. Alonso, *J. Phys. Chem. C*, 2016, **120**, 17357–17364.
26 V. B. Parambhath, R. Nagar and S. Ramaprabhu, *Langmuir*, 2012, **28**, 7826–7833.
27 R. Juarez-Mosqueda, A. Mavrandonakis, A. B. Kuc, L. G. M. Pettersson and T. Heine, *Front. Chem.*, 2015, **3**, 1–9.
28 Z. M. Ao and F. M. Peeters, *J. Phys. Chem. C*, 2010, **114**, 14503–14509.

29 E. Rangel and E. Sansores, *Int. J. Hydrogen Energy*, 2014, **39**, 6558–6566.
30 A. Granja, J. A. Alonso, I. Cabria and M. J. Lopez, *RSC Adv.*, 2015, **5**, 47945–47953.
31 C. M. Ramos-Castillo, J. U. Reveles, R. R. Zope and R. de Coss, *J. Phys. Chem. C*, 2015, **119**, 8402–8409.
32 H. Gao, L. Song, W. Guo, L. Huang, D. Yang and F. Wang, *Carbon*, 2012, **50**, 4476–4482.
33 H. Wang, T. Maiyalagan and X. Wang, *ACS Catal.*, 2012, **2**, 781–794.
34 Y. Shao, S. Zhang, M. H. Engelhard, G. Li, G. Shao and Y. Wang, *J. Mater. Chem.*, 2010, **20**, 7491–7496.
35 Z. Luo, S. Lim, Z. Tian, J. Shang, L. Laia and B. MacDonald, *J. Mater. Chem.*, 2011, **21**, 8038–8044.
36 D. Deng, X. Pan, L. Yu, Y. Cui, Y. Jiang and J. Qi, *Chem. Mater.*, 2011, **23**, 1188–1193.
37 J. J. Zhou, Q. Chen, Y. Han and S. Zheng, *RSC Adv.*, 2015, **5**, 91363–91371.
38 R. Lu, Q. Li, A. R. Botello-Méndez, T. Hayashi, B. Wang, A. Berkdemir, Q. Hao, A. L. Elías, R. Cruz-Silva, H. R. Gutiérrez, Y. Ahm Kim, H. Muramatsu, J. Zhu, M. Endo, H. Terrones, J. C. Charlier, M. Pan and M. Terrones, *Sci. Rep.*, 2012, **2**, 586–593.
39 R. G. Parr and W. Yang, *Density-Functional Theory of Atoms and Molecules*, Oxford University Press, New York, United States, 1989.
40 P. Giannozzi, S. Baroni, N. Bonini, M. Calandra, R. Car, C. Cavazzoni, D. Ceresoli, G. L. Chiarotti, M. Cococcioni, I. Dabo, A. Dal Corso, S. de Gironcoli, S. Fabris, G. Fratesi, R. Gebauer, U. Gerstmann, C. Gougoussis, A. Kokalj, M. Lazzeri, L. Martin-Samos, N. Marzari, F. Mauri, R. Mazzarello, S. Paolini, A. Pasquarello, L. Paulatto, C. Sbraccia, S. Scandolo, G. Sclauzero, A. P. Seitsonen, A. Smogunov, P. Umari and R. M. Wentzcovitch, *J. Phys.: Condens. Matter*, 2009, **21**, 395502.
41 N. Troullier and J. L. Martíns, *Phys. Rev. B: Condens. Matter Mater. Phys.*, 1991, **43**, 1993–2006.
42 X. Gonze, P. Kackell and M. Scheffler, *Phys. Rev. B: Condens. Matter Mater. Phys.*, 1990, **41**, 12264–12267.
43 J. P. Perdew, K. Burke and M. Ernzerhof, *Phys. Rev. Lett.*, 1996, **77**, 3865–3868.
44 J. Zheng, Y. Zhao and D. G. Truhlar, *J. Chem. Theory Comput.*, 2009, **5**, 808–821.
45 F. Karlický, P. Lazar, M. Dubecký and M. Otyepka, *J. Chem. Theory Comput.*, 2013, **9**, 3670–3676.
46 J. Heyd and G. E. Scuseria, *J. Chem. Phys.*, 2004, **121**, 1187–1192.
47 D. Sheppard, R. Terrell and G. Henkelman, *J. Chem. Phys.*, 2008, **128**, 134106.
48 S. Kattel, P. Atanassov and B. Kiefer, *J. Phys. Chem. C*, 2012, **116**, 8161–8166.
49 Y.-X. Yu, *Phys. Chem. Chem. Phys.*, 2013, **15**, 16819–16827.
50 I. Cabria, M. J. López and J. A. Alonso, *Phys. Rev. B: Condens. Matter Mater. Phys.*, 2010, **81**, 035403.
51 I. Cabria, M. J. López, S. Fraile and J. A. Alonso, *J. Phys. Chem. C*, 2012, **116**, 21179–21189.
52 G. J. Kubas, *Acc. Chem. Res.*, 1998, **21**, 120–128.
53 V. A. Borodin, T. T. Vehviläinen, M. G. Ganchenkova and R. M. Nieminen, *Phys. Rev. B: Condens. Matter Mater. Phys.*, 2011, **84**, 075486.

